Heliyon 10 (2024) e38850

Contents lists available at ScienceDirect

Heliyon

journal homepage: www.cell.com/heliyon

Research article

Machine learning model based on dynamic contrast-enhanced ultrasound assisting LI-RADS diagnosis of HCC: A multicenter diagnostic study

Meiqin Xiao [a,b,1], Yishu Deng [b,c,d,1], Wei Zheng [a,b,1], Lishu Huang [e,f,1], Wei Wang [g], Hao Yang [a,b], Danyan Gao [a,b], Zhixing Guo [a,b], Jianwei Wang [a,b], Chaofeng Li [b,d,**], Fang Li [e,f,***], Feng Han [a,b,*,2]

[a] Department of Ultrasound, Sun Yat-sen University Cancer Center, Guangzhou, China
[b] State Key Laboratory of Oncology in South China, Guangdong Provincial Clinical Research Center for Cancer, Sun Yat-sen University Cancer Center, Guangzhou, China
[c] School of Electronics and Information Technology, Sun Yat-sen University, Guangzhou, China
[d] Department of Information, Sun Yat-sen University Cancer Center, Guangzhou, China
[e] Department of Ultrasound, Chongqing University Cancer Hospital, School of Medicine, Chongqing University, Chongqing, China
[f] Chongqing Key Laboratory for Intelligent Oncology in Breast Cancer (iCQBC), Chongqing University Cancer Hospital, Chongqing, China
[g] Department of Medical Ultrasonics, Institute of Diagnostic and Interventional Ultrasound, The First Affiliated Hospital of Sun Yat-sen University, Guangzhou, China

ARTICLE INFO

Keywords:
Ultrasonography
Hepatocellular carcinoma
Image enhancement
Dynamic contrast-enhanced ultrasound
Liver imaging reporting and data system
Machine learning
Quantitative ultrasound
Time-intensity curve

ABSTRACT

Background: To enhance the accuracy of hepatocellular carcinoma (HCC) diagnosis using contrast-enhanced (CE) US, the American College of Radiology developed the CEUS Liver Imaging Reporting and Data System (LI-RADS). However, the system still exhibits limitations in distinguishing between HCC and non-HCC lesions.
Purpose: To investigate the viability of employing machine learning methods based on quantitative parameters of contrast-enhanced ultrasound for distinguishing HCC within LR-M nodules.
Materials and methods: This retrospective analysis was conducted on pre-treatment CEUS data from liver nodule patients across multiple centers between January 2013 and June 2022. Quantitative analysis was performed using CEUS images, and the machine learning diagnostic models based on quantitative parameters were utilized for the classification diagnosis of LR-M nodules. The performance of the model was assessed using the area under the receiver operating characteristic curve (AUC) and compared with the performance of four radiologists.

Abbreviations: AUC, area under the receiver operating characteristic curve; CE, contrast-enhanced; DCEUS, dynamic contrast-enhanced ultrasound; HCC, hepatocellular carcinoma; LI-RADS, Liver Imaging Reporting and Data System; ML, Machine Learning; RF, Random Forest Classifier; ROC, receiver operating characteristic; ROI, the region of interest; SVC, Support Vector Classifier; TIC, time-intensity curves; XGBoost, eXtreme Gradient Boosting Classifier.

* Corresponding author. Department of Ultrasound, Sun Yat-sen University Cancer Center, Guangzhou, China.
** Corresponding author. Department of Information, Sun Yat-sen University Cancer Center, Guangzhou, China.
*** Corresponding author. Department of Ultrasound, Chongqing University Cancer Hospital, School of Medicine, Chongqing University, Chongqing, China.
E-mail addresses: lichaofeng@sysucc.org.cn (C. Li), lifang0703@cqu.edu.cn (F. Li), hanfeng@sysucc.org.cn (F. Han).
[1] These authors contributed equally.
[2] Lead contact.

https://doi.org/10.1016/j.heliyon.2024.e38850
Received 6 July 2024; Received in revised form 9 September 2024; Accepted 1 October 2024
Available online 2 October 2024

Results: The training and internal testing datasets comprised 168 patients (median age, 53 years [IQR, 18 years]), while the external testing datasets from two other centers included 110 patients (median age, 54 years [IQR, 16 years]). In the internal independent test set, the top-performing Random Forest model achieved an AUC of 0.796 (95%CI: 0.729–0.853) for diagnosing HCC. This model exhibited a sensitivity of 0.752 (95%CI: 0.750–0.755) and a specificity of 0.761 (95%CI: 0.758–0.764), outperforming junior radiologists who achieved an AUC of 0.619 (95%CI: 0.543–0.691, $p < .01$) with sensitivity and specificity of 0.716 (95%CI: 0.713–0.718) and 0.522 (95%CI: 0.519–0.526), respectively.
Conclusion: Significant differences in contrast-enhanced ultrasound quantitative parameters are observed between HCC and non-HCC lesions. Machine learning models leveraging these parameters effectively distinguish HCC categorized as LR-M, offering a valuable adjunct for the accurate classification of liver nodules within the CEUS LI-RADS framework.

1. Introduction

According to 2020 statistics from CA: *A Cancer Journal for Clinicians*, primary liver cancer is the sixth most common malignant tumor worldwide and ranks third in cancer-related deaths [1]. In China, liver cancer ranks fourth in terms of incidence and is the second leading cause of cancer-related deaths, predominantly affecting men. This places a substantial burden on China's healthcare system and significantly contributes to cancer mortality rates [2]. Hepatocellular carcinoma (HCC), the most common pathological type of primary liver cancer [3,4], can be diagnosed through standalone imaging examinations, eliminating the need for biopsy confirmation [5,6]. Early detection and timely intervention can lead to favorable prognoses and extended survival times for most HCC patients through locoregional therapy or resection [7]. Some patients may even achieve a cure through orthotopic liver transplantation [8–10]. Numerous studies have suggested that early detection and accurate diagnosis significantly reduce mortality and extend life expectancy [11,12]. Therefore, the imaging diagnosis of HCC is particularly important [13,14].

The 2017 version of the American College of Radiology's Contrast-Enhanced (CE) US Liver Imaging Reporting and Data System (LI-RADS) included a category called LR-M, which indicates lesions that are probably or definitely malignant but not specific to HCC [15,16]. A primary objective of the LR-M category is to maintain the specificity of HCC diagnosis within the LI-RADS algorithm while ensuring sensitivity in detecting malignant tumors [14]. Several studies have demonstrated that approximately 56 % (95 % CI: 44%–69 %) of lesions categorized as LR-M were HCC, with this proportion increasing to 75 % for nodules measuring $\leq$20 mm [17–22]. This finding underscores the limitations of LI-RADS in terms of sensitivity. Given the distinct treatment strategies and prognoses for HCC and non-HCC lesions, particularly non-HCC malignancies [23,24], this issue could lead to an increased frequency of liver biopsies. Studies have shown that adjusting the time criterion for early washout (less than 60 s) and the time criterion for marked washout (within 2 min) can enhance the specificity of HCC diagnosis [25–27]. Additionally, supplementary CEUS features may assist in distinguishing ICC classified as LR-M from HCC with atypical imaging characteristics [28–30].

Previous studies have demonstrated that the quantitative analysis of dynamic contrast-enhancement US (DCEUS) using standardized software can reveal additional information that might be overlooked during purely visual assessments, potentially enhancing the accuracy of tumor perfusion and blood flow evaluation [31–34]. Concurrently, machine learning can evaluate and diagnose based on novel and complex features [35]. Machine learning models utilizing patient-related data offer a new non-invasive diagnostic tool for clinical applications. To date, the added value of integrating DCEUS with machine learning into the LI-RADS has not been assessed. This study aims to develop a diagnostic model that incorporates quantitative contrast-enhanced ultrasound parameters to assist the LI-RADS and assess its diagnostic performance in distinguishing HCC from non-HCC lesions within the LR-M category.

2. Materials and Methods

This is a multicenter, retrospective study that utilized ultrasound image datasets from three hospitals in China and obtained approval from the Institutional Review Board (Approval No: B2023-320-01). For traceability for anonymous ultrasound images, informed consent was waived.

2.1. Patient selection

Data for the training and internal test set were gathered from the Sun Yat-Sen University Cancer Center (SYSUCC). We retrospectively searched the SYSUCC medical record database from January 2013 to April 2021 to identify patients with untreated hepatic nodules who underwent CEUS. The inclusion and exclusion criteria are outlined in Appendix E1.

Images for the independent external test set were retrospectively obtained from two hospitals: the First Affiliated Hospital of Sun Yat-Sen University (FAH-SYSU), Guangzhou, China (July 2014 to November 2018), and Chongqing University Cancer Hospital (CUCH), Chongqing, China (March 2020 to June 2022). When multiple lesions are observed in a patient, inclusion in the study depends on the completeness and diagnostic clarity of the lesion imaging data. The image was excluded if there was a disagreement between the image and the pathology report regarding the location of the nodule. All data were de-identified before model developing and evaluating. The process diagram illustrating the research process is depicted in Fig. 1.

2.2. DCEUS examination

The ultrasound images were generated using various models of ultrasound equipment produced by seven different manufacturers. The detailed process of CEUS is described in Appendix E2. All images were read by two readers (W.Z. and J.W., each with 7–8 years of experience) to ensure that all enrolled liver nodules were classified as LR-M. In cases of disagreement, a third reader (F.H., with over 15 years of experience) reviewed the images to make the final decision.

The contrast-enhanced ultrasound quantitative software, Sonotumor VMware Workstation 12 pro (vision 12.5.7 build-5813279), was used to retrospectively analyze the dynamic images of different liver nodules within 60 s from the beginning of enhancement to draw the time-intensity curves (TIC) and calculate the required quantitative parameters. The software facilitates the standardization of the quantification process. After uploading dynamic video clips, the software's calibration—considering the ultrasound system, probe, presets, and gain settings—along with motion compensation, ensures reproducibility of results independent of the ultrasound equipment used. The selection of the region of interest (ROI) for both the lesion and the reference area, along with their corresponding TIC, is depicted in Fig. 2. Following the framework for optimal arterial lesion identification, the tumor ROI is defined within the target lesion, comprising at least 20 % of the entire lesion, while avoiding large blood vessels, necrotic areas, and lesion edges (Fig. 2A and C, the green box). The reference ROI is typically defined in the literature as the peripheral normal liver parenchyma at a depth similar to that of the lesion ROI, commonly referred to as the parenchymal equivalent ROI (Fig. 2A and C, yellow box). These signals are subsequently refined through a parameter model to depict the dynamics of the pill. Optimal fit optimization is performed with improved empirical normal distribution. Twelve TIC parameters were defined and extracted from the tumor and liver parenchyma ROIs segmented from 1-min CEUS dynamic images. These include time-related parameters (PT, WiMTT, WoMTT, PX), intensity-related parameters (WiAUC, WoAUC, AUC-all, PX-AUC, PI), and combination parameters (WIPI, WIR, PX-rate) [36]. These parameters translate changes in blood flow and volume, providing a quantitative assessment and comparative analysis of tumor and liver tissue perfusion. Detailed definitions and calculation methods are provided in Fig. 3 and eTable 2.

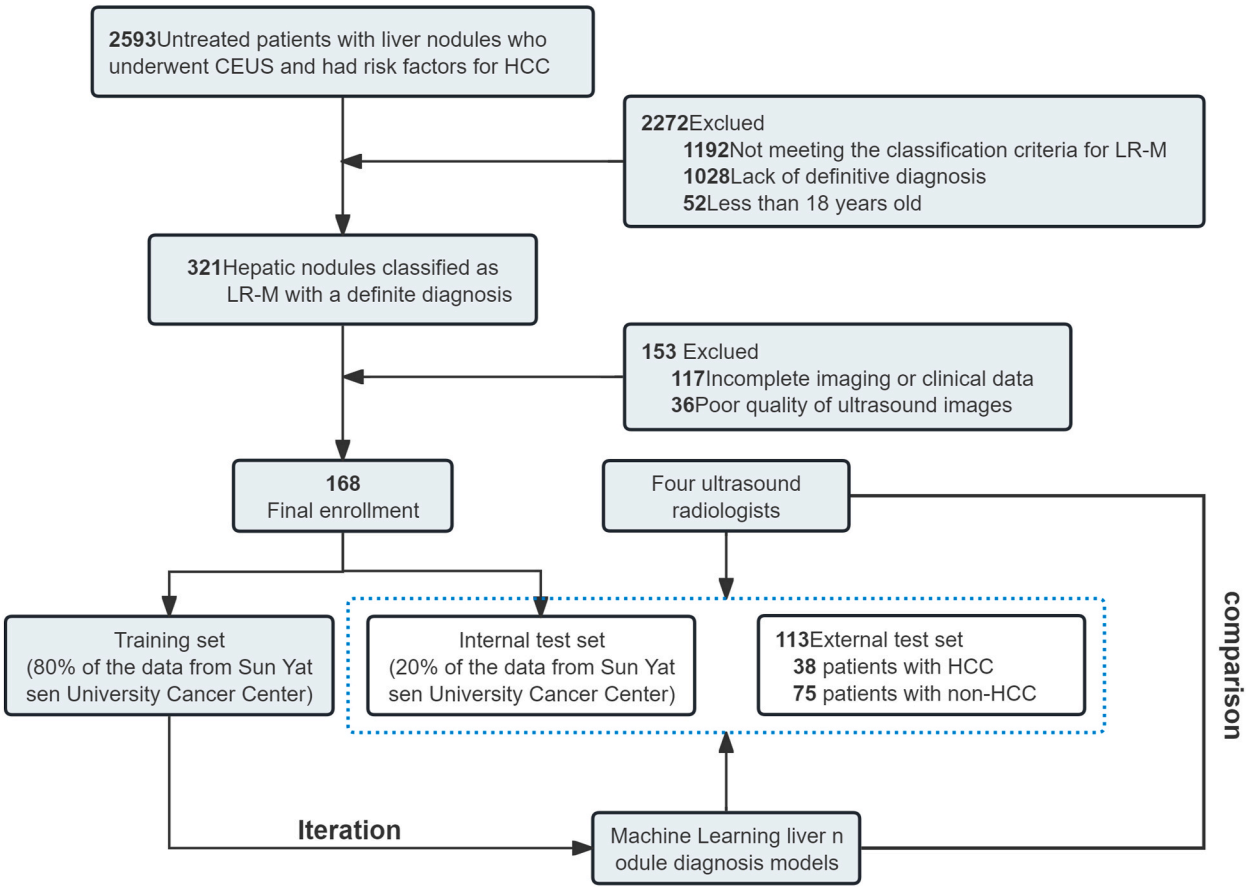

Fig. 1. Flow diagram of the study. *The classification criteria were based on CEUS Liver Imaging Reporting and Data System (LI-RADS) version 2017. HCC = hepatocellular carcinoma, non-HCC = Nodules excluding HCC.

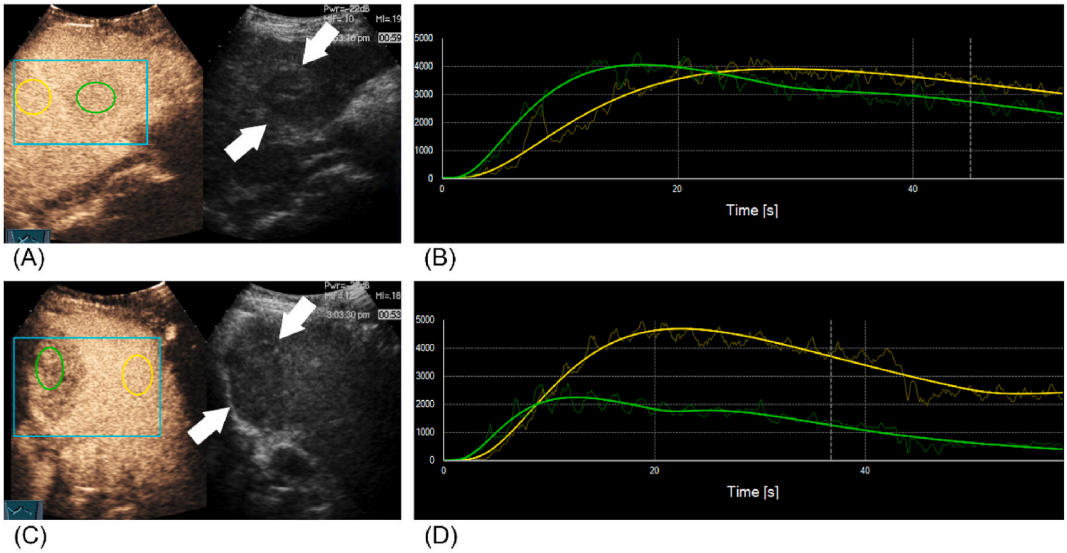

Fig. 2. ROI selection and TIC of different lesions. **(A, B)** Images of a 68-year-old man displaying a nodule classified as LR-M and confirmed as hepatocellular carcinoma through surgery. **(A)** A 4.2 × 3.2 cm hypo-echoic nodule (arrowheads) in segment 6 of the right liver lobe is evident on the surveillance ultrasound (US) image, demonstrating early wash-out (<60 s; timer, 00:59) but presenting mild washout in the contrast-enhanced (CE) US images of the nodule (highlighted by the green box). **(B)** Representative curves of HCC derived from quantitative analysis software. **(C, D)** Images of a 62-year-old woman showing a nodule classified as LR-M and confirmed as liver metastases biopsy. **(C)** A 7.2 × 4.6 cm hypo-echoic nodule (arrowheads) in segment 7 of the right liver lobe is observed on the surveillance US image, indicating early wash-out (<60 s; timer, 00:48) but more marked washout in the CEUS images of the nodule (highlighted by the green box). **(D)** Typical curves of non-HCC lesions obtained from quantitative analysis software. (For interpretation of the references to color in this figure legend, the reader is referred to the Web version of this article.)

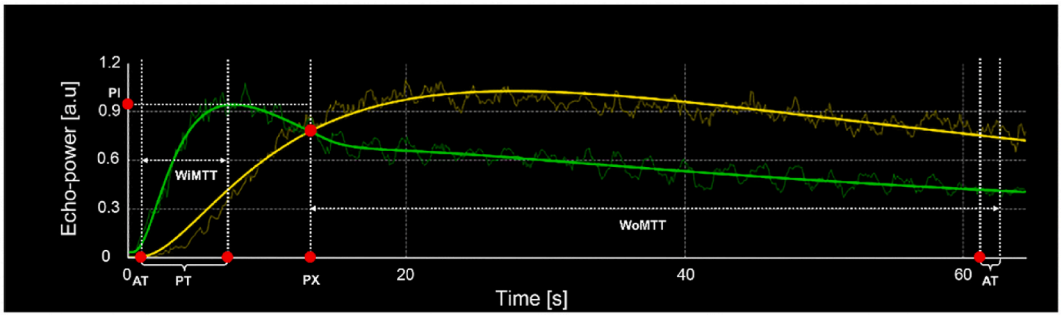

Fig. 3. The definitions of the quantitative parameters (The data in this example has been normalized). The X axis is the time, and the Y axis is the enhancement intensity. The TIC of the target tissues is shown in green, and the liver parenchyma is shown in yellow, where the elongated curve corresponds to the original video signal intensity and the re-curve is fitted. The linearized signal displays echo-power data over time, showing how the intensity of the reflected echoes changes as a function of time. AT: Arrival time; PI: Peak intensity; PT: Peak time; PX: Time at the intersection of the TIC; WiMTT: Mean transit time of the wash-in segmen; WoMTT: Mean transit time of the was-out segment. (For interpretation of the references to color in this figure legend, the reader is referred to the Web version of this article.)

2.3. Reference standard

Histological examination or the combination of clinical and imaging reference standards were used to diagnose all nodules. The demonstration of arterial phase hyperenhancement and wash-out appearance in the portal venous phase or delayed phase by extracellular CECT or MRI in nodules larger than 1 cm is the comprehensive criterion for HCC [5,10,13,37]. Characteristic characteristics on images taken with at least two CE imaging modalities and objective evidence of additional nodules during follow-up in patients with known primary extrahepatic cancer and a partial or complete response to chemotherapy were used as metastatic criteria. Histological examination diagnosed all other non-HCC cancers.

2.4. Clinical interpretation of US images

To obtain the reader's diagnostic performance on the independent test set, a cohort of four radiologists was employed, including two junior radiologists with 1–3 years of experience and two senior radiologists with 8 years of experience. Each radiologist independently reviewed the ultrasound images and associated clinical information for liver nodules, with all radiologists remaining blinded to both the pathological confirmation of nodule status and the study's objectives to prevent bias. The diagnostic process involved each radiologist making a dichotomous classification of the nodules as either HCC or non-HCC based on the provided data. To ensure consistency and accuracy, consensus meetings were conducted to resolve any disagreements, and the inter-rater agreement was assessed to maintain diagnostic reliability.

2.5. Machine learning Model and statistical analysis

Using ICC, Pearson, and Lasso methods for feature selection, three key features were incorporated into the model: WoMTT_A, WiAUC_A, and PX-rate. Subsequently, to enhance the stability and generalization performance of the models, the intensity values of the lesion and reference regions for each case were standardized. The standardized values were then utilized for modeling. The standardized intensity values, denoted by x_{std}, are defined as

$$x_{std} = \frac{x}{\max(x_{\_R})} \tag{1}$$

where x represents the original intensity values, and $\max(x_{\_R})$ is the maximum intensity within the reference ROI for the same case.

Using the selected and standardized parameters, the diagnostic performance of three key supervised machine learning binary classification models for HCC—Random Forest (RF), Support Vector Classifier (SVC), and eXtreme Gradient Boosting (XGBoost)—was assessed [38]. The model's stability and generalizability were ensured and validated through five-fold cross-validation and a multi-center external testing strategy. The model assesses the likelihood of HCC based on CEUS parameters, comparing its diagnoses to pathology or clinical findings and radiologists' assessments. ROC curves were generated for each test set, and AUC values were calculated. Diagnostic metrics (accuracy, sensitivity, specificity, PPV, NPV) were derived from confusion matrices, and the 95 % confidence intervals (CI) of each value were calculated using the method described by Robert Newcombe, derived from a procedure outlined by E. B. Wilson in 1927 [39]. The comparison between AUCs was performed using the method designed by DeLong et al. [40]. F1 scores were also reported. Statistical analysis was performed using SPSS 26.0, with significance set at $p < .05$. Modeling was done in Python 3.6.

3. Results

3.1. Participants and liver Observations

As presented in Table 1, CEUS data for the training and internal test sets were sourced from the liver imaging database of SYSUCC, encompassing 176 nodules from 168 patients who underwent CEUS examinations between January 2013 and April 2021. An external test dataset comprising 113 nodules from 110 patients was sourced from the liver imaging databases of FAH-SYSU (July 2014 to November 2018) and CUCH (March 2020 to June 2022). The training and the internal independent test set included 127 men (75.6 %,

Table 1
Patient and Nodule characteristics.

Variable	Training and internal test sets		External test sets	
Patients	168		110	
No. of men	127	(75.6)	71	(64.5)
Age (y)[a]	53	(18)	54	(16)
No. of nodules	176		113	
Nodule size				
< 19 mm	20	(11.4)	8	(7.1)
20 ~ 49 mm	90	(51.1)	50	(44.2)
≥50 mm	66	(37.5)	55	(48.7)
Histological examination	116	(65.9)	113	(100)
Diagnosis				
Hepatocellular carcinoma	109	(61.9)	38	(33.6)
Intrahepatic cholangiocarcinoma	22	(12.5)	28	(24.8)
Combined hepatocellular-cholangiocarcinoma	3	(1.7)	3	(2.6)
Metastasis	38	(21.6)	40	(35.4)
Other malignancies	1	(0.6)	2	(1.8)
Inflammatory lesions	2	(1.1)	1	(0.9)
Other benign nodules	1	(0.6)	1	(0.9)

Note. —Data in parentheses are percentages unless otherwise noted.
[a] Data are medians, with IQRs in parentheses.

median age, 53 years [IQR, 18 years]). The external independent test set contained 71 men (64.5 %, median age, 54 years [IQR, 16 years]).

The nodules in the training and internal test sets were confirmed either by histological evaluation (n = 116, 65.9 %) or by a combination of clinical and imaging reference standards (n = 60, 34.1 %). All nodules in the external test set were confirmed by histologic evaluation. In total, 61.9 % (109 of 176) of the lesions in the training and internal test set were HCC, 36.4 % (64 of 176) were non-HCC malignancies, and 1.7 % (3 of 176) were benign lesions. Non-HCC malignancies included 38 (21.6 %) liver metastases, 22 (12.5 %) intrahepatic cholangiocarcinoma, 3 (1.7 %) combined hepatocellular-cholangiocarcinoma, and 1 (0.6 %) small cell neuroendocrine carcinoma. Benign lesions included 2 (1.1 %) inflammatory lesions and 1 (0.6 %) intrahepatic intraductal papillary tumor with high-grade intraepithelial neoplasia. Details of the external test dataset from each center are provided in eTable 1.

3.2. Quantitative analysis with CEUS

Table 2 presents the results of quantitative CEUS parameters for HCC and non-HCC lesions. Statistically significant differences were observed in PT, PE, WoMTT, WiAUC, WoAUC, AUC-all, WIPI, PX, PX-AUC, and PX-rate ($p < .001$, for all). No statistically significant differences were found in WiMTT and WIR ($p = .06$ and 0.15, respectively).

3.3. Performance of machine learning models

The machine learning models demonstrated strong performance in diagnosing liver nodules using quantitative ultrasound parameters across both internal and external test sets. In the internal test set, the RF model achieved an AUC of 0.796 (95 % CI: 0.729–0.853), which is comparable to the AUCs of the XGBoost model (0.786; 95 % CI: 0.718–0.845) and the SVC model (0.804; 95 % CI: 0.738–0.860). Statistical comparisons (RF vs XGBoost, RF vs SVC, and XGBoost vs SVC) showed non-significant differences ($p = .86$, 0.86, and 0.35, respectively). For the external test set, the AUC was 0.768 (95 % CI: 0.741–0.794) for the RF model, 0.779 (95 % CI: 0.742–0.812) for the XGBoost model, and 0.825 (95 % CI: 0.791–0.856) for the SVC model (RF vs XGBoost, RF vs SVC, and XGBoost vs SVC with p-values of 0.68, <0.001, and <0.001, respectively, which were statistically different). On the internal test set, the XGBoost model achieved the highest accuracy at 0.761 (95%CI: 0.759–0.763), followed closely by the RF model at 0.755 (95%CI: 0.754–0.758), while the SVC model had a slightly lower accuracy of 0.744 (95%CI: 0.742–0.746).The sensitivities were 0.752 (95%CI: 0.750–0.755) for the RF model, 0.788 (95%CI: 0.787–0.791) for the XGBoost model, and 0.743 (95%CI: 0.740–0.746) for the SVC model; and the specificities were 0.761 (95%CI: 0.758–0.764), 0.716 (95%CI: 0.713–0.720), and 0.746 (95%CI: 0.743–0.750), respectively. On the external set, the accuracies were 0.807 (95%CI: 0.775–0.840) for the RF model, 0.798 (95%CI: 0.797–0.799) for the XGBoost model, and 0.788 (95%CI: 0.787–0.789) for the SVC model; the sensitivities were 0.647 (95%CI: 0.579–0.715), 0.653 (95%CI: 0.650–0.655), and 0.600 (95%CI: 0.598–0.602); and the specificities were 0.888 (95%CI: 0.856–0.920), 0.872 (95%CI: 0.871–0.873), and 0.883 (95%CI: 0.882–0.884), respectively. Overall, in comparison to the other two models, the RF model exhibited the best performance (Table 3).

The performance of the machine learning model was further benchmarked against that of radiologists. As shown in Table 3, on the internal test set, the RF model achieved an AUC of 0.796 (95 % CI: 0.729–0.853), significantly outperforming junior radiologists (AUC: 0.619, 95 % CI: 0.543–0.691; $p < .001$), and demonstrating comparable performance to senior radiologists (AUC: 0.756, 95 % CI: 0.685–0.817; $p = .41$). Senior radiologists achieved an accuracy of 0.761 (95%CI: 0.759–0.763), sensitivity of 0.780 (95%CI: 0.777–0.782), and specificity of 0.731 (95%CI: 0.728–0.735), while junior radiologists reported lower metrics at 0.642 (95%CI: 0.640–0.644), 0.716 (95%CI: 0.713–0.718) and 0.522 (95%CI: 0.519–0.526), respectively. Similarly, on the external test set, the RF model's AUC (0.768, 95%CI: 0.741–0.794)) exceeded that of junior radiologists (0.669, 95%CI: 0.574–0.754; $p = .04$) and matched senior radiologists' AUC (0.781, 95%CI: 0.694–0.854; $p = .91$). Senior radiologists achieved an accuracy of 0.779 (95%CI: 0.776–0.781), sensitivity of 0.789 (95%CI: 0.785–0.794), and specificity of 0.773 (95%CI: 0.770–0.776), compared to 0.664 (95%CI:

Table 2
Quantitative parameters in the regions of interest (ROIs) of 109 hepatocellular carcinomas and 67 non-HCC.

Parameters ($\bar{\chi} \pm SD$)	ROI						t	p-value
	HCC			non-HCC				
PT	7.43	±	3.00	5.99	±	2.33	3.34	<0.001
PE	0.81	±	0.12	0.72	±	0.13	4.37	<0.001
WiMTT	2.23	±	0.87	1.98	±	0.84	1.91	0.06
WoMTT	81.22	±	49.92	46.90	±	22.40	6.22	<0.001
WiAUC	4.19	±	1.82	2.93	±	1.33	4.90	<0.001
WoAUC	31.73	±	6.65	23.82	±	7.96	7.10	<0.001
AUC-all	35.91	±	7.17	26.75	±	8.58	7.63	<0.001
WIPI	0.56	±	0.08	0.49	±	0.10	5.19	<0.001
WIR	0.15	±	0.10	0.17	±	0.08	−1.44	0.15
PX	12.83	±	4.17	10.77	±	2.90	3.86	<0.001
PX-AUC	28.08	±	5.87	21.93	±	7.70	5.61	<0.001
PX-rate	26.83	±	13.14	43.45	±	16.61	−7.36	<0.001

Note. —The data presented in the table are normalized.

Table 3
The diagnostic performance of three ML models and radiologists based on the test set.

	ML models			Radiologists	
	RF	XGBoost	SVC	Senior	Junior
Internal independent test set					
AUC	0.796 (0.729–0.853)	0.786 (0.718–0.845)	0.804 (0.738–0.860)	0.756 (0.685–0.817)	0.619 (0.543–0.691)
accuracy	0.755 (0.754–0.758)	0.761 (0.759–0.763)	0.744 (0.742–0.746)	0.761 (0.759–0.763)	0.642 (0.640–0.644)
sensitivity	0.752 (0.750–0.755)	0.788 (0.787–0.791)	0.743 (0.740–0.746)	0.780 (0.777–0.782)	0.716 (0.713–0.718)
specificity	0.761 (0.758–0.764)	0.716 (0.713–0.720)	0.746 (0.743–0.750)	0.731 (0.728–0.735)	0.522 (0.519–0.526)
PPV	0.837 (0.834–0.839)	0.819 (0.817–0.821)	0.827 (0.824–0.829)	0.825 (0.823–0.828)	0.709 (0.706–0.712)
NPV	0.654 (0.650–0.657)	0.676 (0.673–0.680)	0.641 (0.638–0.644)	0.671 (0.668–0.675)	0.530 (0.526–0.534)
F1	0.792	0.804	0.783	0.802	0.712
p-value	…	…	…	.41[a]	<.001[b]
External independent test set					
AUC	0.768 (0.741–0.794)	0.779 (0.742–0.812)	0.825 (0.791–0.856)	0.781 (0.694–0.854)	0.669 (0.574–0.754)
accuracy	0.807 (0.775–0.840)	0.798 (0.797–0.799)	0.788 (0.787–0.789)	0.779 (0.776–0.781)	0.664 (0.661–0.666)
sensitivity	0.647 (0.579–0.715)	0.653 (0.650–0.655)	0.600 (0.598–0.602)	0.789 (0.785–0.794)	0.684 (0.679–0.689)
specificity	0.888 (0.856–0.920)	0.872 (0.871–0.873)	0.883 (0.882–0.884)	0.773 (0.770–0.776)	0.653 (0.650–0.657)
PPV	0.746 (0.679–0.812)	0.721 (0.719–0.723)	0.722 (0.719–0.724)	0.638 (0.634–0.643)	0.500 (0.496–0.504)
NPV	0.833 (0.796–0.869)	0.832 (0.831–0.833)	0.813 (0.812–0.814)	0.879 (0.876–0.881)	0.803 (0.800–0.806)
F1	0.693	0.685	0.655	0.706	0.578
p-value	…	…	…	.91[a]	.04[b]

Note. —The values in parentheses represent the 95 % confidence interval. AUC = area under the receiver operating characteristic curve. F_1 = a weighted average used to measure the PPV and sensitivity. NPV = negative predictive value. PPV = positive predictive value.
[a] Comparison of diagnostic performance between senior radiologists and the RF model.
[b] Comparison of diagnostic performance between junior radiologists and the RF model.

0.661–0.666), 0.684 (95%CI: 0.679–0.689), and 0.653 (95%CI: 0.650–0.657) for junior radiologists.

Fig. 4 illustrates ROC curves comparing model performance with radiologists of varying experience levels. Within this figure, points representing the specificity and sensitivity of radiologists' diagnostic performance on the test set are graphed within the model's ROC curve. Notably, Fig. 4 illustrates that across both internal and external test sets, points denoting the performance of junior radiologists fall below the model's ROC curve and lie outside their respective 95 % confidence intervals. Conversely, the diagnostic proficiency of senior radiologists closely mirrors that of the model. The machine learning model exhibited superior performance compared to junior radiologists in diagnosing HCC using quantitative parameters derived from CEUS of liver nodules, and this difference held statistical significance.

3.4. Interpretability of machine learning models

SHapley Additive exPlanations (SHAP) values were utilized in this study to identify and interpret the impact of each feature on the model's predictive outcomes. Using the RF model as an example, Fig. 5A presents a SHAP summary plot that visualizes the influence of

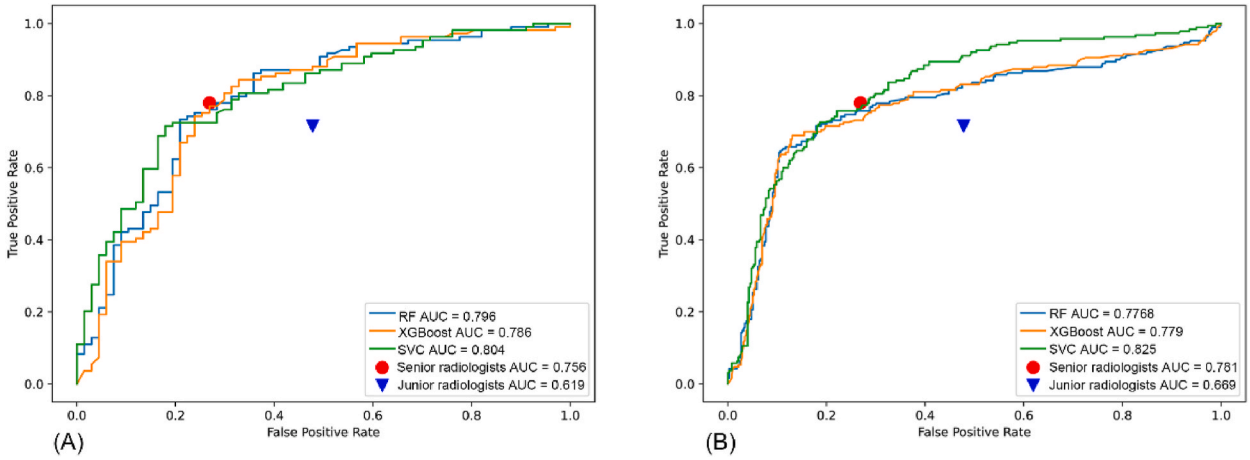

Fig. 4. Diagnostic performance comparison between the ML models and radiologists in HCC identification with liver nodules. **(A)** Diagnostic performance of radiologists and ML models compared within the internal independent testing set. **(B)** Diagnostic performance of radiologists and ML models compared within the external independent testing set. Circles represent the diagnostic sensitivity and specificity of the senior radiologist, while triangles indicate the sensitivity and specificity of the junior radiologist. ML = machine learning. AUC = area under the receiver operating characteristic curve.

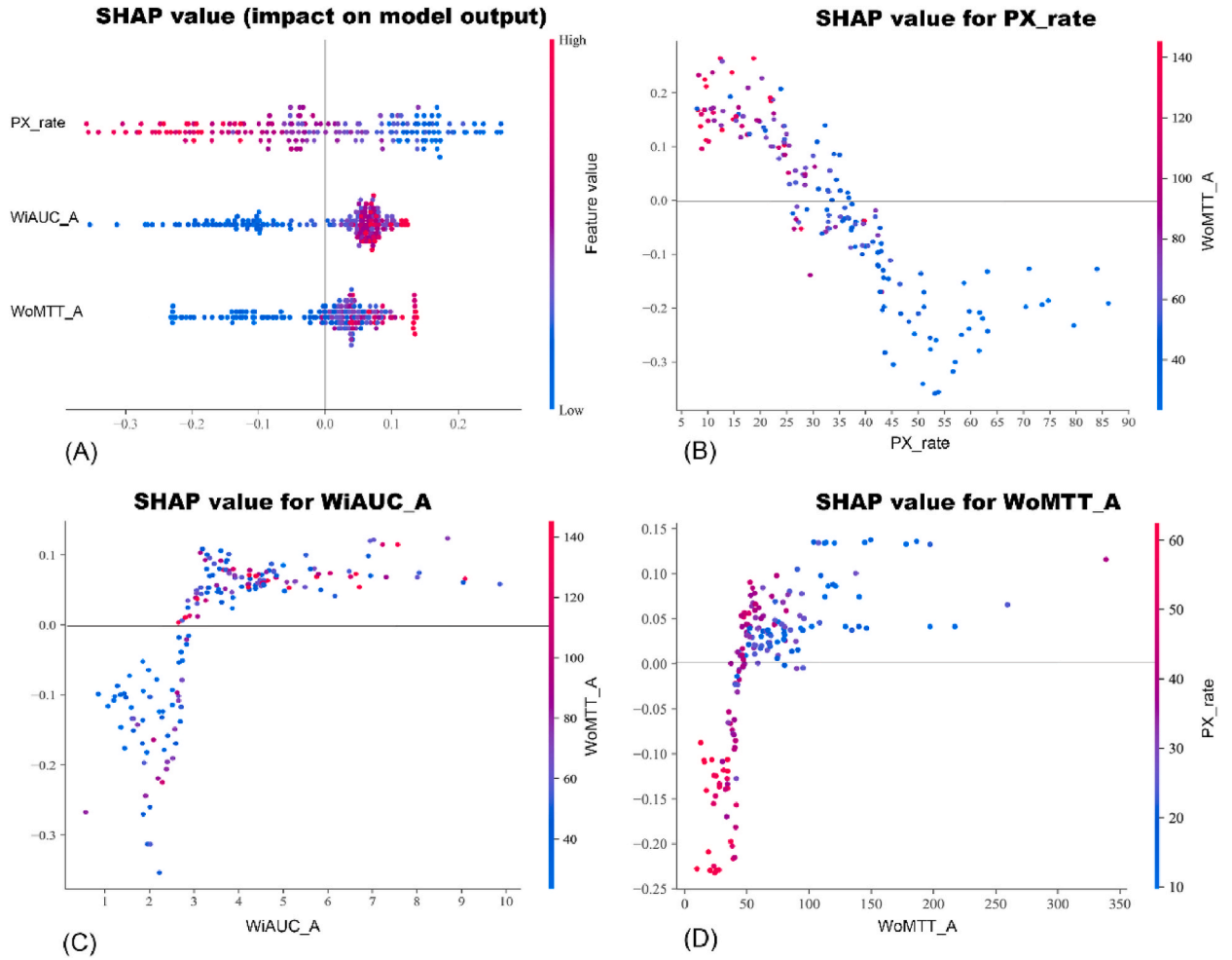

Fig. 5. SHapley Additive exPlanations (SHAP) Summary and Dependency Plots for Key Features. **(A)** The SHAP summary plot. Each dot represents the SHAP value of a specific feature for an individual patient, with multiple dots converging into a violin plot where the width indicates patient density. The color gradient, ranging from blue to red, reflects the variation in feature values from low to high. The Y-axis lists the features, ordered by their average impact on the model's predictions, while the X-axis represents the SHAP value's influence on the model's output. A larger SHAP value correlates with a higher probability of HCC, with positive values indicating a positive impact on the model's prediction and negative values indicating a negative impact. **(B–D)** The SHAP dependency plots. **(B)** PX_rate vs. WoMTT_A. **(C)** WiAUC_A vs. WoMTT_A. **(D)** WoMTT_A vs. PX_rate. The X-axis represents the feature values, while the Y-axis shows the corresponding SHAP values, indicating each feature's contribution to the model output. Each point's color, ranging from red to blue, represents the interacting feature's value from high to low. This color gradient typically reflects the relationship between the primary and interacting features, as well as their combined influence on the model's prediction. (For interpretation of the references to color in this figure legend, the reader is referred to the Web version of this article.)

multiple features on the model's predictions. A larger SHAP value indicates a greater positive impact of the feature on the model's predictions, while the absolute SHAP value reflects the feature's overall importance in the model output. As shown in Fig. 5A, PX_rate had the most significant impact on the model's predictions, followed by WiAUC_A and WoMTT_A. Notably, PX_rate exhibited a negative correlation with the model's predictive values, whereas WiAUC_A and WoMTT_A showed positive correlations. For instance, lower PX_rate values increased the likelihood of a lesion being classified as HCC.

Additionally, SHAP dependency plots illustrated how changes in specific feature values affected the model's predictions and revealed interactions between these features and other important ones (Fig. 5B–D). By observing the color variations in the plot, the relationship between the primary feature and interacting features, as well as their combined effect on the model's predictions, can be understood. For example, in Fig. 5B, PX_rate is negatively correlated with the model's predictive values. When PX_rate is below 20, it positively influences the model's predictions, whereas when PX_rate exceeds 35, it exerts a negative impact. Within the range of 20–40, the SHAP values show minimal variation, indicating that PX_rate has a relatively small influence on the model's predictions in this range. Additionally, it can be observed that as PX_rate decreases, the WoMTT_A value increases, demonstrating a negative correlation between these two features. These examples illustrate that the machine learning model not only provides accurate HCC diagnostic probabilities but also offers valuable insights for distinguishing different liver lesions.

4. Discussion

In this study, dynamic contrast-enhanced ultrasound was used to analyze HCC and non-HCC lesions classified as LR-M. By integrating this approach with machine learning, we successfully developed a diagnostic model for LR-M liver nodules. The leading model demonstrated robust diagnostic capabilities on test sets, achieving an AUC of 0.796 (95CI: 0.729–0.853), sensitivity of 0.752 (95CI: 0.750–0.755), and specificity of 0.761 (95CI: 0.758–0.764) on the internal test set. In both internal and external test sets, the machine learning diagnostic model significantly surpassed junior radiologists ($p = .41$ and 0.91, respectively), while remaining comparable to that of senior practitioners ($p < .001$ and $= 0.04$, separately). These results demonstrate the potential of quantitative ultrasound analysis coupled with machine learning in diagnosing LR-M liver nodules. This approach mitigates the limitations associated with current operator-dependent and visually-based CEUS diagnosis, revealing additional lesion-specific CEUS information. These findings introduce innovative perspectives and methodologies for the differential diagnosis of LR-M nodules, highlighting the transformative impact of integrating quantitative ultrasound and machine learning in clinical practice.

The CEUS LI-RADS, developed by the American College of Radiology, significantly enhances the specificity of HCC diagnosis, achieving a negative predictive value exceeding 98 % [17,18,21,41]. However, distinguishing between HCC and non-HCC malignant lesions remains challenging. Numerous studies indicate a notably low positive predictive value for diagnosing non-HCC malignant lesions within the LR-M category, primarily due to a substantial proportion of HCC cases falling under LR-M, ranging from 44 % to 69 % [17–22]. In our study, the proportion of HCC cases reached 61.9 %. Given the distinct treatment strategies and prognoses for HCC and non-HCC lesions, particularly non-HCC malignancies [23,24], enhancing the sensitivity of HCC diagnosis is crucial. Multiple studies have highlighted the significance of the degree of wash-out in CEUS for identifying malignant tumor characteristics in liver nodules [30,31,41,42]. Compared to HCC, the extent of contrast agent wash-out in intrahepatic cholangiocarcinoma is more pronounced [29,42]. Among LR-M nodules showing arterial phase hyper-enhancement and early mild wash-out (no punched-out appearance within 5 min) on CEUS, 93 % were identified as HCC [41]. In our study, 87.1 % of HCC cases exhibited mild wash-out, which was significantly higher than the proportion observed in non-HCC lesions (40.8 %, $p < .01$). While these CEUS wash-out features provide valuable information for differentiating hepatic malignant lesions, their assessment relies heavily on human visual interpretation, which is operator-dependent and prone to variability. Moreover, qualitative analyses may suffer from data loss due to uncertain individual results.

TIC analysis in CEUS enhances diagnostic precision by providing detailed information beyond visual evaluation, thereby eliminating potential subjectivity and observer bias in clinical diagnosis [33,43]. Previous studies have demonstrated the feasibility of DCEUS in distinguishing between benign and malignant liver lesions [33,44–46]. Our study demonstrates significant differences in parameters including PT, PI, WoMTT, WiAUC, WoAUC, AUC-all, WIPI, PX, and PX-AUC between HCC and non-HCC lesions in LR-M nodules. Additionally, the PX-rate parameter, which characterizes the degree of washout, was innovatively included to overcome the limitations of traditional quantitative parameters, thereby providing a more comprehensive analysis of the TIC. After feature selection, WoMTT_A, WiAUC_A, and PX-rate were identified as the most stable and diagnostically valuable DCEUS quantitative parameters for distinguishing between HCC and non-HCC lesions. The marked increase in WiAUC observed in HCC lesions compared to non-HCC lesions can be attributed to the hypervascularity of HCC. Neovascularization leads to an expansion of the intra-vascular space and a concurrent reduction in interstitial space, thereby causing a substantial enhancement in arterial perfusion [47–49]. In addition, the significant differences in WoAUC and PX-rate further highlight the importance of washout time and degree of wash-out in distinguishing HCC from non-HCC lesions, consistent with our statistical findings and previous studies [31,46,50,51]. However, no significant differences were observed between the wash-in rate parameters, WiMTT, and WIR, suggesting that perfusion rates during the early arterial phase (prior to peak enhancement) may not vary significantly across different lesions. This detailed quantitative approach, combined with machine learning, enhances the accuracy and reproducibility of imaging diagnoses compared to traditional visual assessments.

This study has several limitations. First, potential biases may arise from the selection of retrospective data and the radiologists involved. Data sourced from specialized oncology hospitals may have introduced selection and information biases. Additionally, limitations in the availability and quality of recorded data, including the exclusion of low-quality images, could impact the completeness and accuracy of the data, thereby affecting the potential generalizability of the results. Consequently, larger-scale, multicenter prospective studies are needed to ensure applicability in clinical settings. Secondly, this study focused solely on image analysis and processing, without integrating clinical and pathological information, which could have contributed to a more comprehensive diagnostic model. Ultimately, despite software calibration and data normalization, variability remains in the results. Variations in ultrasound equipment and settings across centers, coupled with differences in operator expertise, may have led to inconsistencies in image quality and contrast enhancement patterns, potentially affecting CEUS image quality. Additionally, the manual selection and delineation of ROIs during processing may have been influenced by the operator's skill and experience. Future prospective studies with standardized imaging protocols are essential to validate these findings and minimize these sources of variability. Furthermore, artificial intelligence-based methods for automatic lesion identification and delineation may help address these challenges.

In conclusion, our demonstration underscores the potential of combining ultrasound imaging with machine learning algorithms for accurate Liver Imaging Reporting and Data System M category (LR-M) liver nodule diagnosis, addressing the limitations within the domain of ultrasound imaging coupled with artificial intelligence. Further validation and model calibration of this DCEUS diagnostic model through extensive, multicenter, prospective studies on a large scale is imperative.

Funding

The research does not have any external funding.

Data and code availability statement

The study's data and code have not been put in a public repository, but they can be obtained from the corresponding author upon reasonable request.

CRediT authorship contribution statement

Meiqin Xiao: Writing – original draft, Visualization, Resources, Project administration, Methodology, Investigation, Formal analysis, Data curation, Conceptualization. **Yishu Deng:** Writing – original draft, Visualization, Validation, Software, Resources, Methodology, Investigation, Data curation. **Wei Zheng:** Writing – review & editing, Methodology, Formal analysis, Conceptualization. **Lishu Huang:** Writing – original draft, Validation, Resources, Methodology, Investigation, Formal analysis, Data curation. **Wei Wang:** Writing – original draft, Validation, Resources, Methodology, Investigation, Formal analysis, Data curation. **Hao Yang:** Writing – original draft, Resources, Methodology, Investigation, Data curation. **Danyan Gao:** Writing – original draft, Resources, Methodology, Investigation, Data curation. **Zhixing Guo:** Writing – original draft, Resources, Project administration, Methodology, Conceptualization. **Jianwei Wang:** Writing – original draft, Supervision, Methodology, Investigation, Conceptualization. **Chaofeng Li:** Writing – review & editing, Supervision, Software, Resources, Project administration, Conceptualization. **Fang Li:** Writing – review & editing, Supervision, Resources, Conceptualization. **Feng Han:** Writing – review & editing, Writing – original draft, Supervision, Resources, Methodology, Formal analysis, Data curation, Conceptualization.

Declaration of competing interest

The authors declare that they have no known competing financial interests or personal relationships that could have appeared to influence the work reported in this paper.

Acknowledgments

The authors are grateful to the patients for participating in this study.

Appendix A. Supplementary data

Supplementary data to this article can be found online at https://doi.org/10.1016/j.heliyon.2024.e38850.

References

[1] H. Sung, J. Ferlay, R.L. Siegel, M. Laversanne, I. Soerjomataram, A. Jemal, F. Bray, Global cancer statistics 2020: GLOBOCAN estimates of incidence and mortality worldwide for 36 cancers in 185 countries, CA Cancer J Clin 71 (2021) 209–249, https://doi.org/10.3322/caac.21660.
[2] B. Han, R. Zheng, H. Zeng, S. Wang, K. Sun, R. Chen, L. Li, W. Wei, J. He, Cancer incidence and mortality in China, 2022, J Natl Cancer Cent 4 (2024) 47–53, https://doi.org/10.1016/j.jncc.2024.01.006.
[3] A. Vogel, T. Meyer, G. Sapisochin, R. Salem, A. Saborowski, Hepatocellular carcinoma, Lancet 400 (2022) 1345–1362, https://doi.org/10.1016/S0140-6736(22)01200-4.
[4] J.M. Llovet, R.K. Kelley, A. Villanueva, A.G. Singal, E. Pikarsky, S. Roayaie, R. Lencioni, K. Koike, J. Zucman-Rossi, R.S. Finn, Hepatocellular carcinoma, Nat Rev Dis Primers 7 (2021) 6, https://doi.org/10.1038/s41572-020-00240-3.
[5] A. Vogel, A. Cervantes, I. Chau, B. Daniele, J.M. Llovet, T. Meyer, J.-C. Nault, U. Neumann, J. Ricke, B. Sangro, P. Schirmacher, C. Verslype, C.J. Zech, D. Arnold, E. Martinelli, ESMO guidelines committee, hepatocellular carcinoma: ESMO clinical practice guidelines for diagnosis, treatment and follow-up, Ann. Oncol. 29 (2018) iv238–iv255, https://doi.org/10.1093/annonc/mdy308.
[6] A.J. Craig, J. von Felden, T. Garcia-Lezana, S. Sarcognato, A. Villanueva, Tumour evolution in hepatocellular carcinoma, Nat. Rev. Gastroenterol. Hepatol. 17 (2020) 139–152, https://doi.org/10.1038/s41575-019-0229-4.
[7] Z.J. Brown, D.I. Tsilimigras, S.M. Ruff, A. Mohseni, I.R. Kamel, J.M. Cloyd, T.M. Pawlik, Management of hepatocellular carcinoma: a review, JAMA Surg 158 (2023) 410–420, https://doi.org/10.1001/jamasurg.2022.7989.
[8] V. Mazzaferro, E. Regalia, R. Doci, S. Andreola, A. Pulvirenti, F. Bozzetti, F. Montalto, M. Ammatuna, A. Morabito, L. Gennari, Liver transplantation for the treatment of small hepatocellular carcinomas in patients with cirrhosis, N. Engl. J. Med. 334 (1996) 693–699, https://doi.org/10.1056/NEJM199603143341104.
[9] M. Reig, A. Forner, J. Rimola, J. Ferrer-Fàbrega, M. Burrel, Á. Garcia-Criado, R.K. Kelley, P.R. Galle, V. Mazzaferro, R. Salem, B. Sangro, A.G. Singal, A. Vogel, J. Fuster, C. Ayuso, J. Bruix, BCLC strategy for prognosis prediction and treatment recommendation: the 2022 update, J. Hepatol. 76 (2022) 681–693, https://doi.org/10.1016/j.jhep.2021.11.018.
[10] European Association for the Study of the Liver, Electronic address: easlofficeeasloffice.eu, European association for the study of the liver, EASL clinical practice guidelines: management of hepatocellular carcinoma, J. Hepatol. 69 (2018) 182–236, https://doi.org/10.1016/j.jhep.2018.03.019.
[11] J.D. Yang, J.K. Heimbach, New advances in the diagnosis and management of hepatocellular carcinoma, BMJ 371 (2020) m3544, https://doi.org/10.1136/bmj.m3544.

[12] H. Zeng, M. Cao, C. Xia, D. Wang, K. Chen, Z. Zhu, R. Fu, S. Zhang, J. Zhou, H. Wang, X. Qi, S. Dai, Y. Chen, Z. Sun, H. Ding, Q. Li, H. Zhao, X. Zhang, J. Morze, J. S. Ji, F. Sun, X. Yu, C. Qu, W. Chen, Performance and effectiveness of hepatocellular carcinoma screening in individuals with HBsAg seropositivity in China: a multicenter prospective study, Nat Cancer 4 (2023) 1382–1394, https://doi.org/10.1038/s43018-023-00618-8.

[13] A.G. Singal, J.M. Llovet, M. Yarchoan, N. Mehta, J.K. Heimbach, L.A. Dawson, J.H. Jou, L.M. Kulik, V.G. Agopian, J.A. Marrero, M. Mendiratta-Lala, D.B. Brown, W.S. Rilling, L. Goyal, A.C. Wei, T.H. Taddei, AASLD Practice Guidance on prevention, diagnosis, and treatment of hepatocellular carcinoma, Hepatology 78 (2023) 1922–1965, https://doi.org/10.1097/HEP.0000000000000466.

[14] V. Chernyak, K.J. Fowler, R.K.G. Do, A. Kamaya, Y. Kono, A. Tang, D.G. Mitchell, J. Weinreb, C.S. Santillan, C.B. Sirlin, LI-RADS: looking back, looking forward, Radiology 307 (2023) e222801, https://doi.org/10.1148/radiol.222801.

[15] American College of Radiology, CEUS LI-RADS v2017 core, Read More (2017). www.acr.org/-/media/ACR/Files/RADS/LI-RADS/CEUS-LI-RADS-2017-Core.pdf. (Accessed 12 February 2022). https://www.ajronline.org/doi/full/10.2214/AJR.22.28420.

[16] Y. Kono, C.B. Sirlin, D.T. Fetzer, T.K. Kim, S.K. Rodgers, F. Piscaglia, A. Lyshchik, C.F. Dietrich, S.R. Wilson, Time to clarify common misconceptions about the liver imaging reporting and data system for contrast-enhanced US, Radiology 295 (2020) 245–247, https://doi.org/10.1148/radiol.2020192557.

[17] Y. Zhou, Z. Qin, J. Ding, L. Zhao, Y. Chen, F. Wang, X. Jing, Risk stratification and distribution of hepatocellular carcinomas in CEUS and CT/MRI LI-RADS: a meta-analysis, Front. Oncol. 12 (2022) 873913, https://doi.org/10.3389/fonc.2022.873913.

[18] E. Terzi, M. Iavarone, M. Pompili, L. Veronese, G. Cabibbo, M. Fraquelli, L. Riccardi, L. De Bonis, A. Sangiovanni, S. Leoni, M.A. Zocco, S. Rossi, N. Alessi, S. R. Wilson, F. Piscaglia, Contrast ultrasound LI-RADS LR-5 identifies hepatocellular carcinoma in cirrhosis in a multicenter restropective study of 1,006 nodules, J. Hepatol. 68 (2018) 485–492, https://doi.org/10.1016/j.jhep.2017.11.007.

[19] S.R. Wilson, A. Lyshchik, F. Piscaglia, D. Cosgrove, H.-J. Jang, C. Sirlin, C.F. Dietrich, T.K. Kim, J.K. Willmann, Y. Kono, Ceus li-rads: algorithm, implementation, and key differences from CT/MRI, Abdom Radiol (NY) 43 (2018) 127–142, https://doi.org/10.1007/s00261-017-1250-0.

[20] J. Ding, Z. Qin, Y. Zhou, H. Zhou, Q. Zhang, Y. Wang, X. Jing, F. Wang, Impact of revision of the LR-M criteria on the diagnostic performance of contrast-enhanced ultrasound LI-RADS, Ultrasound Med. Biol. 47 (2021) 3403–3410, https://doi.org/10.1016/j.ultrasmedbio.2021.08.007.

[21] J. Ding, L. Long, X. Zhang, C. Chen, H. Zhou, Y. Zhou, Y. Wang, X. Jing, Z. Ye, F. Wang, Contrast-enhanced ultrasound LI-RADS 2017: comparison with CT/MRI LI-RADS, Eur. Radiol. 31 (2021) 847–854, https://doi.org/10.1007/s00330-020-07159-z.

[22] J. Li, W. Ling, S. Chen, L. Ma, L. Yang, Q. Lu, Y. Luo, The interreader agreement and validation of contrast-enhanced ultrasound liver imaging reporting and data system, Eur. J. Radiol. 120 (2019) 108685, https://doi.org/10.1016/j.ejrad.2019.108685.

[23] A. Beaufrère, J. Calderaro, V. Paradis, Combined hepatocellular-cholangiocarcinoma: an update, J. Hepatol. 74 (2021) 1212–1224, https://doi.org/10.1016/j.jhep.2021.01.035.

[24] M. Vithayathil, S.A. Khan, Current epidemiology of cholangiocarcinoma in Western countries, J. Hepatol. 77 (2022) 1690–1698, https://doi.org/10.1016/j.jhep.2022.07.022.

[25] W. Ling, M. Wang, X. Ma, T. Qiu, J. Li, Q. Lu, Y. Luo, The preliminary application of liver imaging reporting and data system (LI-RADS) with contrast-enhanced ultrasound (CEUS) on small hepatic nodules ($\leq$ 2cm), J. Cancer 9 (2018) 2946–2952, https://doi.org/10.7150/jca.25539.

[26] J.-Y. Huang, J.-W. Li, W.-W. Ling, T. Li, Y. Luo, J.-B. Liu, Q. Lu, Can contrast enhanced ultrasound differentiate intrahepatic cholangiocarcinoma from hepatocellular carcinoma? World J. Gastroenterol. 26 (2020) 3938–3951, https://doi.org/10.3748/wjg.v26.i27.3938.

[27] D. Zeng, M. Xu, J.-Y. Liang, M.-Q. Cheng, H. Huang, J.-M. Pan, Y. Huang, W.-J. Tong, X.-Y. Xie, M.-D. Lu, M. Kuang, L.-D. Chen, H.-T. Hu, W. Wang, Using new criteria to improve the differentiation between HCC and non-HCC malignancies: clinical practice and discussion in CEUS LI-RADS 2017, Radiol. Med. (2021), https://doi.org/10.1007/s11547-021-01417-w.

[28] L.-D. Chen, S.-M. Ruan, Y. Lin, J.-Y. Liang, S.-L. Shen, H.-T. Hu, Y. Huang, W. Li, Z. Wang, X.-Y. Xie, M.-D. Lu, M. Kuang, W. Wang, Comparison between M-score and LR-M in the reporting system of contrast-enhanced ultrasound LI-RADS, Eur. Radiol. 29 (2019) 4249–4257, https://doi.org/10.1007/s00330-018-5927-8.

[29] H.-L. Guo, X. Zheng, M.-Q. Cheng, D. Zeng, H. Huang, X.-Y. Xie, M.-D. Lu, M. Kuang, W. Wang, M.-F. Xian, L.-D. Chen, Contrast-enhanced ultrasound for differentiation between poorly differentiated hepatocellular carcinoma and intrahepatic cholangiocarcinoma, J. Ultrasound Med. (2021), https://doi.org/10.1002/jum.15812.

[30] Y. Chen, W. Wang, Differentiation between hepatocellular carcinoma and intrahepatic cholangiocarcinoma using contrast-enhanced ultrasound: a systematic review and meta-analysis, Clin. Hemorheol. Microcirc. (2021), https://doi.org/10.3233/CH-211145.

[31] C.F. Dietrich, C.P. Nolsøe, R.G. Barr, A. Berzigotti, P.N. Burns, V. Cantisani, M.C. Chammas, N. Chaubal, B.I. Choi, D.-A. Clevert, X. Cui, Y. Dong, M. D'Onofrio, J. B. Fowlkes, O.H. Gilja, P. Huang, A. Ignee, C. Jenssen, Y. Kono, M. Kudo, N. Lassau, W.J. Lee, J.Y. Lee, P. Liang, A. Lim, A. Lyshchik, M.F. Meloni, J.M. Correas, Y. Minami, F. Moriyasu, C. Nicolau, F. Piscaglia, A. Saftoiu, P.S. Sidhu, I. Sporea, G. Torzilli, X. Xie, R. Zheng, Guidelines and good clinical practice recommendations for contrast-enhanced ultrasound (CEUS) in the liver-update 2020 WFUMB in cooperation with EFSUMB, AFSUMB, AIUM, and FLAUS, Ultrasound Med. Biol. 46 (2020) 2579–2604, https://doi.org/10.1016/j.ultrasmedbio.2020.04.030.

[32] G. Esposto, P. Santini, F. Termite, L. Galasso, I. Mignini, M.E. Ainora, A. Gasbarrini, M.A. Zocco, Dynamic contrast enhanced ultrasound in differential diagnosis of hepatocellular carcinoma: a systematic review and meta-analysis, World J. Gastrointest. Oncol. 16 (2024) 2804–2815, https://doi.org/10.4251/wjgo.v16.i6.2804.

[33] S. Schwarz, D.-A. Clevert, M. Ingrisch, T. Geyer, V. Schwarze, J. Rübenthaler, M. Armbruster, Quantitative analysis of the time-intensity curve of contrast-enhanced ultrasound of the liver: differentiation of benign and malignant liver lesions, Diagnostics 11 (2021) 1244, https://doi.org/10.3390/diagnostics11071244.

[34] R.W. Green, E. Epstein, Dynamic contrast-enhanced ultrasound improves diagnostic performance in endometrial cancer staging, Ultrasound Obstet. Gynecol. 56 (2020) 96–105, https://doi.org/10.1002/uog.21885.

[35] A. Chae, M.S. Yao, H. Sagreiya, A.D. Goldberg, N. Chatterjee, M.T. MacLean, J. Duda, A. Elahi, A. Borthakur, M.D. Ritchie, D. Rader, C.E. Kahn, W.R. Witschey, J.C. Gee, Strategies for implementing machine learning algorithms in the clinical practice of Radiology, Radiology 310 (2024) e223170, https://doi.org/10.1148/radiol.223170.

[36] A.N. Sencha, Y.N. Patrunov (Eds.), Contrast-Enhanced Ultrasound: from Simple to Complex, first ed. 2022 edition, Springer, 2022.

[37] K. Hasegawa, N. Takemura, T. Yamashita, T. Watadani, M. Kaibori, S. Kubo, M. Shimada, H. Nagano, E. Hatano, H. Aikata, H. Iijima, K. Ueshima, K. Ohkawa, T. Genda, K. Tsuchiya, T. Torimura, M. Ikeda, J. Furuse, M. Akahane, S. Kobayashi, H. Sakurai, A. Takeda, T. Murakami, U. Motosugi, Y. Matsuyama, M. Kudo, R. Tateishi, Committee for revision of the clinical practice guidelines for hepatocellular carcinoma, Tokyo, Japan, clinical practice guidelines for hepatocellular carcinoma: the Japan society of hepatology 2021 version (5th JSH-HCC guidelines), Hepatol. Res. 53 (2023) 383–390, https://doi.org/10.1111/hepr.13892.

[38] J.C. Ahn, A. Connell, D.A. Simonetto, C. Hughes, V.H. Shah, Application of artificial intelligence for the diagnosis and treatment of liver diseases, Hepatology 73 (2021) 2546–2563, https://doi.org/10.1002/hep.31603.

[39] E.B. Wilson, Probable inference, the law of succession, and statistical inference, J. Am. Stat. Assoc. 22 (1927) 209–212, https://doi.org/10.2307/2276774.

[40] E.R. DeLong, D.M. DeLong, D.L. Clarke-Pearson, Comparing the areas under two or more correlated receiver operating characteristic curves: a nonparametric approach, Biometrics 44 (1988) 837, https://doi.org/10.2307/2531595.

[41] W. Zheng, Q. Li, X. Zou, J. Wang, F. Han, F. Li, L. Huang, A. Li, J. Zhou, Evaluation of contrast-enhanced US LI-RADS version 2017: application on 2020 liver nodules in patients with hepatitis B infection, Radiology 294 (2020) 299–307, https://doi.org/10.1148/radiol.2019190878.

[42] L. Cerrito, M.E. Ainora, R. Borriello, G. Piccirilli, M. Garcovich, L. Riccardi, M. Pompili, A. Gasbarrini, M.A. Zocco, Contrast-enhanced imaging in the management of intrahepatic cholangiocarcinoma: state of art and future perspectives, Cancers 15 (2023) 3393, https://doi.org/10.3390/cancers15133393.

[43] Y. Iwasa, T. Iwashita, H. Ichikawa, N. Mita, S. Uemura, K. Yoshida, K. Iwata, T. Mukai, I. Yasuda, M. Shimizu, Efficacy of contrast-enhanced harmonic endoscopic ultrasound for pancreatic solid tumors with a combination of qualitative and quantitative analyses: a prospective pilot study, Dig. Dis. Sci. 67 (2022) 1054–1064, https://doi.org/10.1007/s10620-021-06931-5.

[44] M.E. Ainora, L. Cerrito, A. Liguori, I. Mignini, A. De Luca, L. Galasso, M. Garcovich, L. Riccardi, F. Ponziani, F. Santopaolo, M. Pompili, A. Gasbarrini, M. A. Zocco, Multiparametric dynamic ultrasound approach for differential diagnosis of primary liver tumors, Int. J. Mol. Sci. 24 (2023) 8548, https://doi.org/10.3390/ijms24108548.

[45] Q. Lu, X.-L. Zhang, H. Han, B.-J. Huang, H. Ding, W.-P. Wang, Value of perfusion parameters for differentiating hepatocellular carcinoma and liver metastasis with hypervascularity and a normal hepatic background on contrast-enhanced ultrasound imaging, J. Ultrasound Med. 38 (2019) 2601–2608, https://doi.org/10.1002/jum.14957.
[46] Y. Dong, S. Chen, K. Möller, Y.-J. Qiu, X.-Y. Lu, Q. Zhang, C.F. Dietrich, W.-P. Wang, Applications of dynamic contrast-enhanced ultrasound in differential diagnosis of hepatocellular carcinoma and intrahepatic cholangiocarcinoma in non-cirrhotic liver, Ultrasound Med. Biol. 49 (2023) 1780–1788, https://doi.org/10.1016/j.ultrasmedbio.2023.03.026.
[47] J. Rimola, Heterogeneity of hepatocellular carcinoma on imaging, Semin. Liver Dis. 40 (2020) 61–69, https://doi.org/10.1055/s-0039-1693512.
[48] H.M. Low, J.Y. Choi, C.H. Tan, Pathological variants of hepatocellular carcinoma on MRI: emphasis on histopathologic correlation, Abdom Radiol (NY) 44 (2019) 493–508, https://doi.org/10.1007/s00261-018-1749-z.
[49] C. Yao, S. Wu, J. Kong, Y. Sun, Y. Bai, R. Zhu, Z. Li, W. Sun, L. Zheng, Angiogenesis in hepatocellular carcinoma: mechanisms and anti-angiogenic therapies, Cancer Biol Med 20 (2023) 25–43, https://doi.org/10.20892/j.issn.2095-3941.2022.0449.
[50] S. Qiu, J. Ding, Z. Qin, Y. Zhou, H. Zhou, Y. Wang, L. Zhao, X. Jing, Application of DCE-US using the LI-RADS for patients with liver nodules at high risk for hepatocellular carcinoma: a preliminary study and comparison with visual interpretation, Eur. J. Radiol. 155 (2022) 110473, https://doi.org/10.1016/j.ejrad.2022.110473.
[51] D. Wildner, B. Schellhaas, D. Strack, R.S. Goertz, L. Pfeifer, C. Fiessler, M.F. Neurath, D. Strobel, Differentiation of malignant liver tumors by software-based perfusion quantification with dynamic contrast-enhanced ultrasound (DCEUS), Clin. Hemorheol. Microcirc. 71 (2019) 39–51, https://doi.org/10.3233/CH-180378.